P13.202 **DUAL POLARIZATION RADAR WINTER STORM STUDIES SUPPORTING DEVELOPMENT OF NEXRAD-BASED AVIATION HAZARD PRODUCTS**

Earle R. Williams, David J. Smalley, Michael F. Donovan
Robert G. Hallowell, Kenta T. Hood, Betty J. Bennett
MIT Lincoln Laboratory

Raquel Evaristo, Adam Stepanek, Teresa Bals-Elsholz, Jacob Cobb, Jaclyn Ritzman
Valparaiso University

1. INTRODUCTION

A major upgrade of the entire US network of 156 radars to polarimetric capability is currently in progress. One important investment in this upgrade by the Federal Aviation Administration lies in the abatement of the icing hazard to aircraft in winter storms associated with the presence of supercooled water. Accordingly, this study is concerned with the use of polarimetric radar measurements (the C-band radar at Valparaiso University) to investigate the microphysics of Midwestern snowstorms. The icing problem from the radar perspective is deemed difficult from the start because (1) the traditional differential reflectivity (ZDR) radar targets (i.e., large raindrops, see Seliga and Bringi, 1976; Teschl et al., 2008) are generally absent in snowstorms and (2) the supercooled water at the crux of the icing problem is comprised of droplets too small to be detected by microwave radar. Fortunately, other hydrometeors (ice crystals), potentially more anisotropic than raindrops and substantially larger than supercooled cloud droplets, manifest themselves in snowstorms and serve to shed polarimetric light on the cloud microphysics related to the presence/absence of supercooled water. The rather subtle distinction between ice supersaturation (without supercooled water) and water saturation (with supercooled water) is of fundamental importance here.

Corresponding Author: Dr. Earle R. Williams, MIT Lincoln Laboratory, 244 Wood Street, Lexington, MA 02420
e-mail: earlew@ll.mit.edu

This work was sponsored by the Federal Aviation Administration (FAA) under Air Force Contract FA8721-05-C-0002. Opinions, interpretations, conclusions, and recommendations are those of the author and are not necessarily endorsed by the United States Government.

2. INTERPRETATIONAL BACKGROUND

2.1 Anisotropy of Hydrometeors - Theoretical Considerations

Historically, differential reflectivity methods were advanced with the promise of better characterization of raindrops and improved measurements of rainfall (Seliga and Bringi, 1976). The anisotropy of gravity-oriented hydrometeors is controlled primarily by their aspect ratio (sometimes called ‘axis ratio’ or ratio of the horizontal to vertical axes). For large raindrops this aspect ratio can reach ~2-3, with associated ZDR values of +5-+7 dB (Teschl et al., 2008).

Ice crystals are substantially smaller than raindrops and so exhibit dramatically smaller reflectivity in general, but their aspect ratios and corresponding ZDR values can greatly exceed those of raindrops. The most anisotropic crystals to radar are the flat (solid) hexagonal plates, and measurement of such crystals in natural clouds show aspect ratios of 20-50 (Auer and Veal, 1970). According to theoretical calculations by Dissanayake et al. (1983), Hogan et al. (2002), and Steinert and Chandra (2009), the ZDR values for such gravity-oriented crystals can reach +9 dB.

Raindrops and solid hexagonal plates are convex shapes whose radar cross sections are well approximated by oblate spheroids with variable aspect ratios. Many other dominant snowstorm hydrometeors have distinctly concave shapes — most notably dendritic crystals and aggregates of crystals otherwise known as snowflakes. Calculations by Vivekanandan et al. (1994) shown in Figure 1 have shown that concavity of shape can strongly dilute the anisotropy and ZDR values. When concave shapes are characterized by their mean volume fraction of ice, the ZDR value of a plate crystal with full volume fraction (1.0) and +9 ZDR has its ZDR diluted to +5 dB for volume fraction 0.5 and to +1 dB for a volume fraction of 0.1.

In this context, Wolde and Vali (2001a), in W-band radar polarimetric measurements from aircraft, have recorded +6 to +7 dB ZDR values on a mixture of plates and sector plates, and +1 to +2 dB values on dendritic crystals. Verified by in situ particle imaging methods, these results provide considerable motivation to use differential reflectivity measurements to characterize snowstorm hydrometeors toward constraining the microphysical situation. The flat plate crystals observed by Wolde and Vali (2001a) were not noticeably rimed, but it is worth noting that the riming of ice crystals can only serve to dilute their anisotropy (by primary thickening of the crystal and reduction of the aspect ratio) and their +ZDR values.

2.2 Temperature and Humidity Control on Ice Crystal Habits

The empirical dependence of ice crystal habit on temperature and humidity is well established on the basis of laboratory measurements with diffusion chambers (Hallett and Mason, 1958; Mason et al., 1963; Bailey and Hallett, 2009), and by observations in natural conditions in winter (Magono and Lee, 1966). Broad consistency is apparent between the two sets of measurements, but greater reliance on the laboratory observations is usually recommended owing to the accurate control on humidity with the diffusion chamber.

Figure 2 shows the latter results from Bailey and Hallett (2009). Routine meteorological observations of humidity do not enable a clear distinction between the conditions of ice saturation and water saturation, a distinction of considerable importance to the crystal habit diagram and to the present study. Figure 2 shows the important water saturation boundary (arcing curve), across which a change in crystal habit is evident for every range of temperature. This diagram is consistent with their more detailed diffusion chamber results. A general empirical feature in all habit diagrams (laboratory and field measurements alike) is the transition for convex crystal shapes (i.e., plates) to concave shapes (i.e., dendrites) from ice supersaturation to water saturation. Based on the considerations of hydrometeor anisotropy in the previous section, one can also expect a substantial diminishment in +ZDR values from the ice supersaturated region to the water supersaturated region.

2.3 Humidity Control by the Lifting Process

In a laboratory environment, ice saturation conditions can be achieved by a static isothermal environment with ice and vapor in equilibrium, and likewise water saturation conditions by an environment with ice, vapor, and supercooled droplets in coexistence. In the real atmosphere, supersaturation is controlled by ascent and adiabatic expansion, competing with vapor condensation and deposition on particles. Korolev and colleagues have given experimental and theoretical attention to the mixed phase conditions in winter storms in a series of papers (Korolev, Isaac and Hallett, 2000; Korolev and Isaac, 2006; Korolev, 2007; Korolev and Field, 2007). Korolev and Mazin (2003) have made theoretical calculations of the full range of possible supersaturation conditions as shown in their Figure 5. Their figure has been adapted for this report as illustrated in Figure 3. Three horizontal lines represent the condition of water saturation for three particular temperatures (-5^{o}C, -15^{o}C, -35^{o}C). The sloping lines represent the steady-state supersaturation for three different updraft speeds (10 m s^{-1},1 m s^{-1}, 10 cm s^{-1}). N is the number concentration of ice crystals (cm^{-3}) and r is the

mean crystal radius (μm). Smaller updraft speeds are needed for a water saturation condition if the crystal population quantity Nr is dilute, because the sink for water vapor in steady state is reduced. If the updraft speed is sufficiently large, water supersaturated conditions and the presence of supercooled water (and hence icing conditions) will prevail. But, a range of updraft speed is also predicted for ice supersaturation without supercooled water in which pristine ice crystals can continue to grow by vapor deposition without riming. For temperatures common to dendritic crystal growth (recall Figure 2), the Korolev and Mazin work suggests a vertical velocity of 10 cm s^{-1} would be necessary.

Occasionally in winter one sees evidence for the glory rings in cold-topped stratocumulus clouds over distances of hundreds to thousands of kilometers in flights with commercial aircraft. The suggestion from Figure 3 is that the ice crystal populations (Nr) are sufficiently small that very modest ascent is able to maintain supercooled water drops (and an icing hazard), essential for the diffraction phenomenon of the glory.

3. OBSERVATIONS

Observations of Midwestern snowstorms have been carried out with the C-band polarimetric radar in Valparaiso, Indiana. The operating characteristics of this radar are P_t = 250 kW, beamwidth = 0.91^o, pulse length 0.8 μsec, wavelength 5.3 cm. A large number of snowstorms have been documented with full volume scans and occasional RHI scans during the 2009, 2010, and 2011 winter season. The two principle storm types have been synoptic/warm frontal progressions from the south and west and the “lake effect” storms due to northerly transport of moisture off Lake Michigan, whose long north-south axis is roughly aligned with the longitude of Valparaiso.

The radar observations in Valparaiso have been supplemented with local thermodynamic soundings (when wind conditions allow) carried out by teams of meteorology students, with principle purpose to document the in situ temperatures at which pronounced anomalies in polarimetric parameters are observed.

3.1 Calibration of Differential Reflectivity

The physical distinctions we have sought to make among snowstorm hydrometeors (as discussed in Section 2.1 for plate crystals, dendrite crystals, and aggregates of crystals (‘snowflakes’)) as summarized in Table 1 and illustrated in Appendix A, Figures A1-A3, require an accuracy in ZDR measurements of a fraction of a decibel (dB). While the stringent 0.1 dB accuracy specification for the new NEXRAD polarimetric capability in ZDR has not been attained for this study, an accuracy in the range of 0.3-0.4 dB has been achieved by making observations with the C-band radar at vertical incidence, when circular cross sections are presented as radar targets. These calibration checks are performed whenever opportunities arise. Figure 4 shows an example of the uniformity of ZDR (right panel) in a vertical profile in stratiform rain from 1-5 km altitude. The offset of ZDR from 0 dB ranges from 0 to 0.3 dB.

3.2 Case Studies

The ZDR observations of winter storms in northern Indiana with the Valparaiso dual pol radar tend to fall in two groups, hereafter referred to as Category A and Category B. The general characteristics of these two groups are summarized in Table 1. The selection of a dominant hydrometeor type in Category A (dendrite crystals) and Category B (plate crystals) is based primarily on the in situ microphysical verifications of Wolde and Vali (2001), with simultaneous polarimetric radar observations. Following this general identification scheme, three selected case studies from each of these two categories have been chosen for presentation and discussion. A common 4-panel display format is used for all cases, including (A) a Plan Position Indicator (PPI) display of radar reflectivity Z (upper left), (B) a PPI of differential reflectivity ZDR (upper right), (C) the inferred atmospheric temperature on the PPI surface based on a proximity thermodynamic sounding (lower left) and

(D) a scatter plot (lower right) of Z versus ZDR from individual range bins within a selected range-limited sector with a red boundary as illustrated in panels A-C. For the selected cases, a representative PPI is presented that best highlights the feature of interest. Often the feature is most prominent in one PPI but is also evident in adjacent PPIs of a full radar volume scan but with less magnitude due to the relationship of the available radar scanning angles to the ambient structure of the atmosphere being sensed.

Table 1 Categorization of Microphysical Regimes

Ice-supersaturated conditions	**Water-saturated conditions**	**Ice- or water-saturated conditions**
Plate crystals (Category B)	**Dendrite crystals (Category A)**	**Aggregates of crystals**
Patches and edges	+ZDR 'bright band' layers	Not evident as distinct feature
Weaker updraft	Stronger updraft	Strong updraft (if riming)
Small reflectivity (-10 to +10 dBZ)	Larger reflectivity (10 to 30 dBZ)	Largest reflectivity (20 to 30 dBZ)
Large +ZDR (+4 dB to +8 dB)	Weak +ZDR (+1 to +3 dB)	Weakest +ZDR (0 to +2 dB)
No icing hazard	Icing hazard	Possible icing hazard

3.2.1 December 8, 2009 2357 UTC; 14.0^{o} PPI: Category A

Category A behavior is well illustrated by this case in Figure 5. The storm at this time features a double melting layer as evident in the sonde temperature plot (C) and Figure 5a, and the two melting layer transitions occur at about 1.95 km altitude (radar range 8 km) and very near the surface. Also evident to the west of the radar at 20 km range in the ZDR plot (B) is the +ZDR 'bright band' anomaly. The Category A feature is located about 4.8 km above ground level (AGL) where temperatures are around -15^{o}C. ZDR values peak at a bit over +3.5 dB in an area of reflectivity around 20 dBZ. These conditions are represented in the crystal habit diagram as dendrites in a water saturated environment. A sense of the depth of this icing hazard layer can be estimated. For this feature, the depth is 2 – 3 km with a 12^{o}C temperature spread. Tracking this feature with time can give an indication of the atmosphere's ability to sustain the hazard.

3.2.2 February 24, 2010 1859 UTC; 4.3^{o} PPI: Category A

This warm frontal snowstorm with atmospheric temperature everywhere <0^{o}C and illustrated in Figure 6 shows evidence for a distinct positive ZDR anomaly (+2 dB) in a ring segment of the PPI to the east of the radar. The in situ temperature there is -13^{o}C, compatible with the idea that dendritic crystals, growing near water saturation in ascending air over a large area, are the dominant ZDR targets. The maximum reflectivity in this +ZDR 'bright band' is 20-25 dBZ, consistent with the general characteristics for a Category A feature. This case also illustrates the common absence of a ring over the full 360 degrees of azimuth, and some evidence for 'spiraling' of the anomalous feature is apparent, suggesting that temperature is not a unique function of altitude

everywhere within radar surveillance, and that isotherms within these storms can be sloping. Also visible in the western margins of the reflectivity and ZDR fields is evidence for Category B behavior: some of the largest +ZDR values (+4 dB) are found in weak reflectivity (<0 dBZ).

3.2.3 August 27, 2011 0043 UTC; 8.0° PPI: Category A

Hurricane Irene forged a path up the east coast of the United States making its first landfall near the Morehead City, NC dual pol NEXRAD. This provided an unprecedented opportunity to study the dual pol signatures from within an Atlantic Basin tropical cyclone. From Figure 7, the tropical nature of the storm is evident through observation of the traditional melting layer 'bright band' signature in the reflectivity (plot A). At about 30 km range, a ring of near 45 dBZ reflectivity is seen about the radar. This feature corresponds to a melting layer altitude of around 4.2 km AGL. This traditional melting layer 'bright band' is also evident at the same range in the differential reflectivity (plot B) as a relative enhancement (about 1 – 2 dB above adjacent areas). At farther range, the Category A +ZDR anomaly is seen as a secondary enhanced ring feature. The multiple banding has been observed in a wide variety of situations. The +ZDR anomaly range (~55 km) relates to an altitude of around 7.9 km AGL. This is an altitude substantially greater than noted in winter storms. This may be surprising to some but clearly the upper reaches of the tropical storm are enveloped in a snowstorm. The nature of that snowstorm is revealed in Figure 7 through plots C and D. The +ZDR anomaly is located in an area near -13°C temperature (from the National Weather Service 00 UTC sounding) with ZDR predominantly +1 – +3 dB and reflectivity of 10 – 25 dBZ. Thus, this bears the same Category A characteristics of a water-saturated environment with dendrite crystals likely being rimed.

3.2.4 January 8, 2010 1625UTC; 4.3° PPI: Category B

Figure 8 illustrates features of a lake effect storm south of Lake Michigan (see lake boundary in Figure) which is relatively compact (with a PPI width of only ~30 km) in comparison with the warm frontal storms of synoptic scale (Feb. 24, 2010, Feb. 1, 2011) also included as case studies. The ZDR anomaly for this storm manifests itself as a distinct edge effect, or 'cocoon', around the entire periphery of the storm, with maximum values reaching +5 to +6 dB. The confinement of inferred anisotropic crystals to the periphery of this convective snow storm suggests the presence of weaker updrafts there than in the core. The in situ temperature in this boundary region is approximately -12°C, which according to the crystal habit diagram in Figure 2 is a region favorable for the occurrence of plate crystals, the most anisotropic hydrometeors following the discussion in Section 2.1. The Z-ZDR scatter plot shows a characteristic inverse relationship, suggesting the idea that the weakest reflectivity is associated with relatively isolated pristine crystals growing at ice supersaturation and without the anisotropy-diluting effects of riming and aggregation. Some tendency for negative values of ZDR is evident at the high reflectivity end of the scatter plot. It is possible that these values are associated with conical graupel (Knight and Knight, 1973), more prevalent in the central, stronger-updraft region of the storm.

3.2.5 November 5, 2010 0514 UTC; 10.0° PPI: Category B

This is a warm case at the surface near the radar (over 5°C), and is illustrated in Figure 9. Convective lake effect rain showers are occurring at the surface but aloft the classic 'cocoon' feature is observed in the ephemeral outer reach of the showers to the south. The expected inverse relationship of ZDR to Z is again noted in the scatter plot (D). ZDR values to near +6 dB are present in the analysis sector in weak reflectivity (near 0 dBZ) suggesting crystal plates in a water subsaturated environment.

3.2.6 February 1, 2011 1912 UTC; 4.3° PPI: Category B

This Ground Hog's Day blizzard produced Chicago's 3rd greatest snowfall on record (20.2

inches) and its synoptic scale overlaid all of northern Indiana as well. Figure 10 illustrates the situation as the northern radar boundary of this storm approaches during the afternoon of February 1. This leading boundary was formed by lifting of air translating north and east along the sloping warm frontal surface whose surface manifestation was still well to the south. A distinct large area patch (~500 km^2) in the northeastern radar quadrant exhibits a +ZDR anomaly reaching +7 dB, among the largest values observed in all storms considered. The anomalous region is also associated with an engulfment in the reflectivity field, suggesting intrusion of drier air and possibly suppressing the attainment of a water saturation condition. Like other Category B cases, the strongest ZDR values are associated with the weakest reflectivities. The in situ temperatures (-6^o to -14^{o}C) are compatible with the suggestion that crystal plates and sector plates are the dominant radar target in the region of weaker reflectivity.

4. DISCUSSION

This study places new radar polarimetric observations of winter storms in the broader context of earlier lab studies on crystal habits (Bailey and Hallett, 2009) and on earlier field observations in which crystal habits were observed in situ along with simultaneous ZDR measurements (Wolde and Vali, 2001a). The new observations on winter storms (and on recent Hurricane Irene) find consistency with warm season studies of stratiform precipitation systems with deep ice regions aloft (Bader et al., 1987; Andric et al., 2009; Moisseev et al., 2009), where local snowstorms are also present. In all of these systems, the most pronounced positive anomalies in differential reflectivity are placed in two Categories A and B (Table 1), both represented by flat thin crystals (dendrites (A) and plates (B)) that orient horizontally in the gravity field, but distinguished by the humidity condition (water-saturated (A) versus ice-supersaturated (B)), and with an associated contrast in ZDR values. The microphysical scenarios in Categories A and B are represented in Appendix A, Figures A2 and A1, respectively. Crystal plates are substantially more anisotropic than dendrites and the dilution in +ZDR for dendrites increases with their "porosity", following theoretical predictions (Vivekanandan et al., 1994; Figure 1). Theoretical limits for ZDR (+9 dB for hexagonal flat plates and ~+5 dB for dendrites) are not achieved in all likelihood because the ice particles in the real atmosphere do not conform (e.g., Stoellinga et al., 2007) to the simplicity and symmetry in the static thermodynamic condition of the diffusion chamber, and because the real atmosphere is turbulent and the crystals are not precisely gravity-aligned. Still these observations show +ZDR values substantially larger than what can be achieved by large raindrops in warmer conditions (Seliga and Bringi, 1976; Teschl et al., 2008).

For ice crystals to dominate the radar reflectivity (and hence the ZDR), at centimeter wavelengths, they must grow to diameters of hundreds of microns by the diffusion of water vapor. It is well established (Byers , 1965) that such growth is governed by a contrast in vapor density over water and over ice (at water-saturated conditions) and this contrast is greatest in a temperature range (-10^o to -20^{o}C) over which flat plates and dendrites are also prevalent (Figure 2), and vanishes at the limits of the so-called "mixed phase" range. This optimal range of temperature for development of large flat crystals is consistent with the in situ temperatures found for ZDR anomalies in this study, and in other work by Sauvageot et al. (1986) and Kennedy and Rutledge (2011). The ZDR 'bright bands' documented here and elsewhere (Hall et al., 1984; Herzegh et al., 1986; Bader et al., 1987, Andric et al., 2009; Moisseev et al., 2009) are notably thicker than the conventional radar bright band at 0^{o}C because a range of temperatures favorable to flat crystal shapes is involved (Figure 2).

A key microphysical distinction with obvious practical importance for aircraft icing is the inferred presence of liquid water in Category A and its required absence in Category B. This study has shown that Category A is a common occurrence in snowstorms in northern Indiana, particularly those of the warm frontal variety. The presence of Category A +ZDR 'bright band' with inferred

supercooled water in cloud layers extending for tens and hundreds of kilometers in winter storms is of obvious concern to aviation. Within a few years time, such layers will be evident in NEXRAD radar displays throughout the continental United States, and so it is essential that aircraft measurements with sensitive detection capability for cloud water are carried out in such layers to verify the association between layered anomalies in ZDR and the possible icing hazard. Category A involves a rather delicate balance between having sufficient liquid water to guarantee water saturation and consequently dendrite crystals, but not having so much water that the dendrite anisotropy is diluted by riming. Both Wolde and Vali (2001a) and Takahashi (2010) have identified conditions of water saturation when the cloud droplets were too small for riming.

The theoretical calculations illustrated in Figure 3 show that thresholds in updraft speed must be crossed to attain the Category A condition, and that plausibly smaller ascent speeds on storm radar edges are needed for Category B. These predictions are fundamental for the assessment of icing hazard in conditions of ascent, but unfortunately the key parameters (updraft and Nr) are not accessible to remote observations. Figure 3 shows that the larger the ice crystal parameter Nr, the larger the updraft threshold, consistent with the picture that the ice particles are sinks for the water vapor that the updraft serves to maintain the supersaturation by adiabatic expansion. In a few cases, in situ aircraft measurements of Nr are available in cloud regions under surveillance for differential reflectivity (Bader et al., 1987; Wolde and Vali, 2001; Hogan et al., 2002), and in which evidence for Category A is present. The measured values fall in the range of 2-5 cm^{-3} μm, as indicated by the grey-shaded region in Figure 3, requiring updraft speeds of the order of 0.1 m s^{-1} for the Category A condition with supercooled water (for an in situ temperature of $-15^{o}C$). Although aircraft measurements of ascent speed in the range of <1 m s^{-1} are difficult to achieve by any observational method, the profilers at long wavelength that backscatter energy from the air itself are probably best suited. In this context, it is interesting to note that updraft speeds with a 50 MHz profiler in the ice regions of stratiform anvils in mesoscale convective systems are in the range of 0.1 to 0.2 m s^{-1} (Williams and Ecklund, 1992; Cifelli and Rutledge, 1994). Good measurements of ascent speeds in snowstorms are not presently known to us, but are essential in assessing icing hazard from first principles.

In addition to the main focus on snowstorms in this study, brief attention has also been given to identifying the +ZDR 'bright band' in the trailing stratiform regions of summertime squall lines, where snowstorms are also underway aloft and ice particles are abundant. Some attention has also been given to identifying such features in the large West African squall lines (Russell et al., 2009) with X-band polarimetric radar (M. Gosset, F. Cazanave and A. Protat, personal communication, 2010) during the 2010 Megha-Tropique field campaign in Niger. In general, the +ZDR bright band is absent or quite weak in these systems. This finding may be the result of dilution of hydrometeor anisotropy by crystal riming and/or aggregation, or by the 'mixed bag' of more isotropic ice particles (i.e., graupel) advected into the stratiform region from the leading deep convection. More work is needed on stratiform systems for which both the vertical motion and the cloud microphysics are well documented.

5. SUMMARY

The impetus for this study of the interpretation of dual polarization parameters is to support development of an automated, radar-based icing hazard product for aviation from the NEXRAD network. Observations of winter storms with the Valparaiso University polarimetric C-band radar and, recently, with the dual pol NEXRAD observations of Hurricane Irene demonstrate the potential to glean valuable clues about the icing hazard. Importantly, the observations have been consistent between radar platforms and with the foundational tenets of cloud and precipitation microphysics.

Two icing hazard related categories were described. Category A, the +ZDR 'bright band'

anomaly, represents a potential icing hazard where dendritic crystals grow in a water saturated environment at temperatures between -10^{o} and -20^{o}C. Category B, the 'cocoon' or edge of storms, represents the non-icing region where plate crystals grow by diffusion in the absence of supercooled water but also in the same temperature range as Category A. A third situation occurs where icing hangs in the balance and is characterized by aggregates (snowflakes) with possible light riming.

The findings to date suggest a coarse ability to confidently distinguish icing from non-icing regions within the confines of a radar volume. Theory and empirical results from controlled environments identify the key factors for segregating these regions to be the combination of vapor density over water and ice, updraft speed and its sustainment, temperature, and ice nuclei concentration. The dual polarimetric parameters reflect the condition of that combination but do not directly measure any of them. In situ evidence suggests the icing hazard more accurately might be portrayed as a blotchy, dynamic environment rather than a laminar, heterogeneous one.

The challenge ahead is to migrate from a coarse to higher fidelity rendering of the icing hazard within the radar volume context. This will be achieved through continued analysis of many more storms particularly as the NEXRAD network converts to a dual pol capability. Collaborations with in situ probing and ground-based complementary sensor networks within view of dual pol radars should further the connection between the radar returns and the physics of icing in the atmosphere.

6. ACKNOWLEDGEMENTS

Discussions with the following individuals contributed much to this work: K. Aydin, L. Carey, F. Cazanave, S. Cohn, M. Gosset, A. Illingworth, J. Hallett, P. Herzegh, A. Khain, A. Korolev, V. Melnikov, A. Protat, D. Rosenfeld, A. Ryzhkov, S. Rutledge, T. Takahashi, D. Van de Kamp, M. Weber, M. Wolde, and D. Zrnic. Also recognized are the dual polarization and winter weather subject matter experts at NSSL and NCAR that are partners with MIT Lincoln Laboratory for the FAA's NEXRAD algorithm program led by T. Webster and B. Bumgarner.

7. REFERENCES

Andric, J., D. Zrnic and V. Melnikov, Two-layer patterns of enhanced ZDR in clouds, 34th Conf. on Radar Meteorology, American Meteorological Society, Williamsburg, VA, 2009.

Auer, A.A. and D.L. Veal, The dimensions of ice crystals in natural clouds, J. Atmos. Sci., 27, 919-926, 1970.

Bader, M.J., S.A. Clough and G.P. Cox, Aircraft and dual polarization observations of hydrometeors in light stratiform precipitation, Quart. J. Roy. Met. Soc., 133, 491-515, 1987.

Bailey, M.P. and J. Hallett, A comprehensive habit diagram for atmospheric ice crystals: Confirmation from the laboratory, AIRS II and other field studies, J. Atmos. Sci., 66, 2888-2899, 2009.

Bringi, V.N. and V. Chandrasekar, *Polarimetric Doppler Weather Radar*, Cambridge University Press, 636 pp. , 2001.

Byers, H.R., *Elements of Cloud Physics*, University of Chicago Press, 191 pp., 1965.

Cifelli, R. and S.A. Rutledge, Vertical motion structure in Maritime Continent mesoscale convective systems: Results from a 50-MHz profiler, J. Atmos. Sci., 51, 2631-2652, 1994.

Dissanayake, A.W., M. Chandra and P.A. Watson, Prediction of differential reflectivity due to various types of ice particles and ice-water mixtures, CAP 83, Norwich, UK, 56–59, IEE Publication No. 219, 1983

Hall, M.P., W.F. Goddard and S.M. Cherry, Identification of hydrometeors and other targets by dual polarization radar, Radio Science, 19, 132-140, 1984.

Hallett, J. and B.J. Mason, The influence of temperature and supersaturation on the habit of

ice crystals grown from the vapor, Proc. Roy. Soc., A247, 440-453, 1958.

Hogan, R.J., A.J. Illingworth, and P.R. Field, Polarimetric radar observations of the growth of highly-aligned ice crystals in the presence of supercooled water, Claire'98 Final Workshop, 167-171, Sept 13-14, 1999, ESA/ESTEC, Noordwijk, Netherlands, 1999.

Hogan, R.J., P.R. Field, A.J. Illingworth, R.J. Cotton, and T.W. Choularton, Properties of embedded convection in warm-frontal mixed-phase cloud from aircraft and polarimetric radar data, Q.J.R.M.S., 128, 451-476, 2002.

Kennedy, P.C. and S.A. Rutledge, S-band dual polarization radar observations in winter storms, J. Appl. Met. And Clim., (in press), 2011.

Knight, C.A. and N.C. Knight, Conical graupel, J. Atmos. Sci., 30, 118-124, 1973.

Korolev, A., G.A. Isaac and J. Hallett, Ice particle habits in stratiform clouds, Q.J.R.M.S., 126, 2873-2902, 2000.

Korolev. A. and I.P. Mazin, Supersaturation of water vapor in clouds, J. Atmos. Sci., 60, 2957-2974, 2003.

Korolev, A. and G.A. Isaac, Relative humidity in liquid, mixed-phase, and ice clouds, J. Atmos. Sci., 63, 2865-2880, 2006.

Korolev, A., Limitations of the Wegener-Bergeron-Findeisen mechanism in the evolution of mixed-phase clouds, J. Atmos. Sci., 64, 3372-3375, 2007.

Korolev, A. and P.R. Field, The effect of dynamics on mixed-phase clouds: Theoretical considerations, J. Atmos. Sci., 65, 66-86, 2007.

Magono, C. and C.W. Lee, Meteorological classification of natural snow crystals, Journal of the Faculty of Science, Hokkaido University, Series VII (Geophysics), Vol. 2, No. 4, 1966.

Mason, B.J., G.W. Bryant and A.P. van den Heuvel, The growth habits and surface structures of ice crystals. Phil. Mag., 8, 505-526, 1963.

Moisseev, D., E. Saltikoff and M. Leskinen, Dual-polarization weather radar observations of snow growth processes, 34th Conf. on Radar Meteorology, American Meteorological Society, Williamsburg, VA, 2009.

Russell, B., E.R. Williams, M. Gosset, F. Cazanave, L. Descroix, N. Guy, T. Lebel, A. Ali, F. Metayer and G. Quantin, Radar/rain-gauge comparisons on squall lines in Niamey, Niger for the AMMA, Quart. J. Roy. Met. Soc., 136, 289-303, 2010.

Sauvageot, H., K. Kouadio and C.-A. Etty, The influence of temperature and supersaturation on the polarization of radar signals, Conference on Radar Meteorology, American Meteorological Society, Snowmass, CO., 173-176, Sept. 22-26, 1986.

Seliga, T.A. and V.N. Bringi, Potential use of radar differential reflectivity measurements at orthogonal polarizations for measuring precipitation, J. Appl. Met., 15, 69-76, 1976.

Steinert, J. and M. Chandra, Classification of ice crystals at C-band, Adv. Eadio Sci., 7, 273-277, 2009.

Stoellinga, M.T., J.D. Locatelli and C.P. Woods, The occurrence of "Irregular" ice particles in stratiform clouds, Notes and Correspondence, J. Atmos. Sci., 64, 2740-2750, 2007.

Takahashi, T., The videosonde system and its use in the study of east asian monsoon rain, Bull. Amer. Met. Soc, 91, 1232-1246, 2010.

Teschl, F., W.L. Randeu, M. Schönhuber, and R. Teschl, Simulation of polarimetric radar variables in rain at S-, C-, and X-band wavelengths, Adv. Geosci., 16, 27-32, 2008.

Vivekanandan, J., V.N. Bringi, M. Hagen and P. Meischner, Polarimetric radar studies of atmospheric ice particles, IEEE Transactions on Geoscience and Remote Sensing, 32, 1-9, 1994.

Williams, E. and W. Ecklund, 50 MHz profiler observations of trailing stratiform precipitation: Constraints on microphysics and in situ charge separation, Preprints, 11th Conf. on Clouds and Precipitation, Montreal, Canada, ICCP, Int. Assoc. of Meteor. Atmos. Phys., 754-757, 1992.

Wolde, M., and G. Vali, Polarimetric signatures from ice crystals observed at 95 GHz in winter clouds, Part I: Dependence of crystal form, J. Atmos. Sci., 58, 828-841, 2001a.

Wolde, M., and G. Vali, Polarimetric signatures from ice crystals observed at 95 GHz in winter clouds, Part II: Frequencies of occurrence, J. Atmos. Sci., 58, 842-849, 2001b.

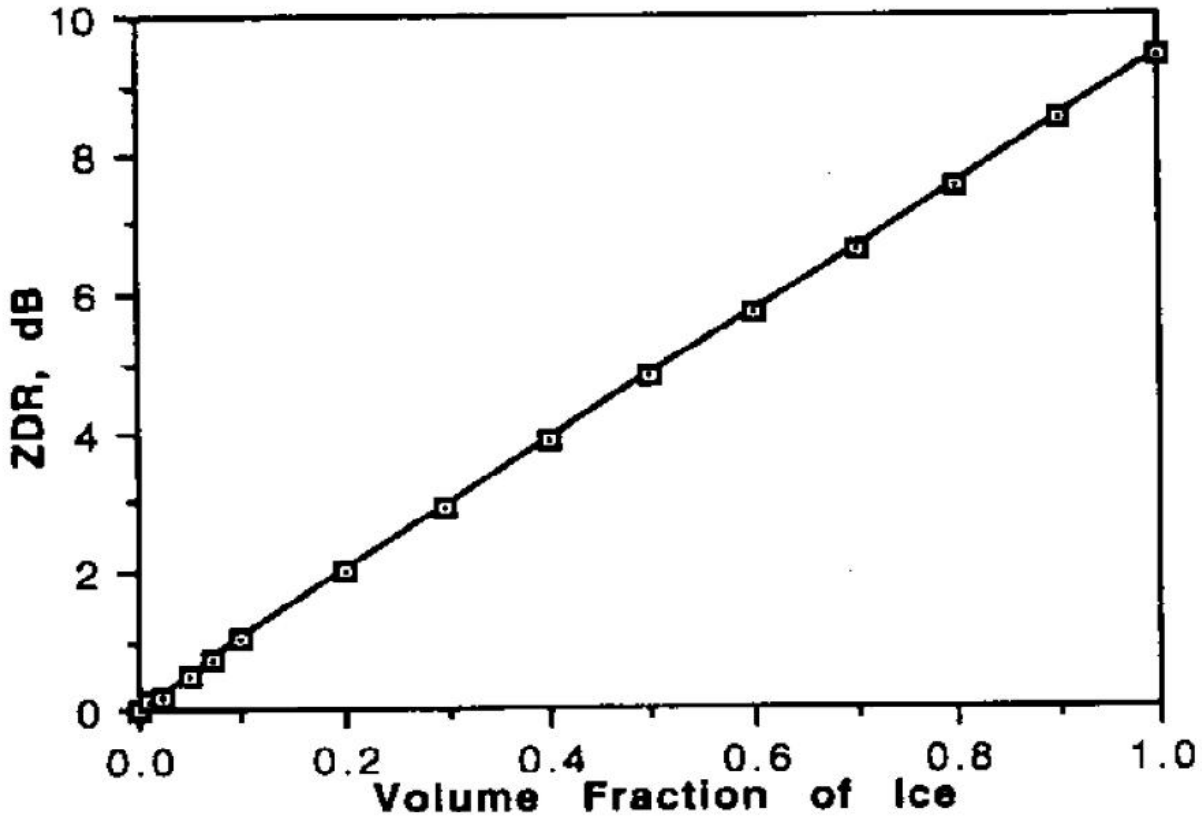

Figure 1. Dilution of differential reflectivity (ZDR) of ice crystals by convex shapes (from Vivekanandan et al. (1994). Solid plate ice crystals (Volume Fraction of Ice of 1) yield significantly higher ZDR than dendrite ice crystals (approx. 0.5 Volume Fraction of Ice).

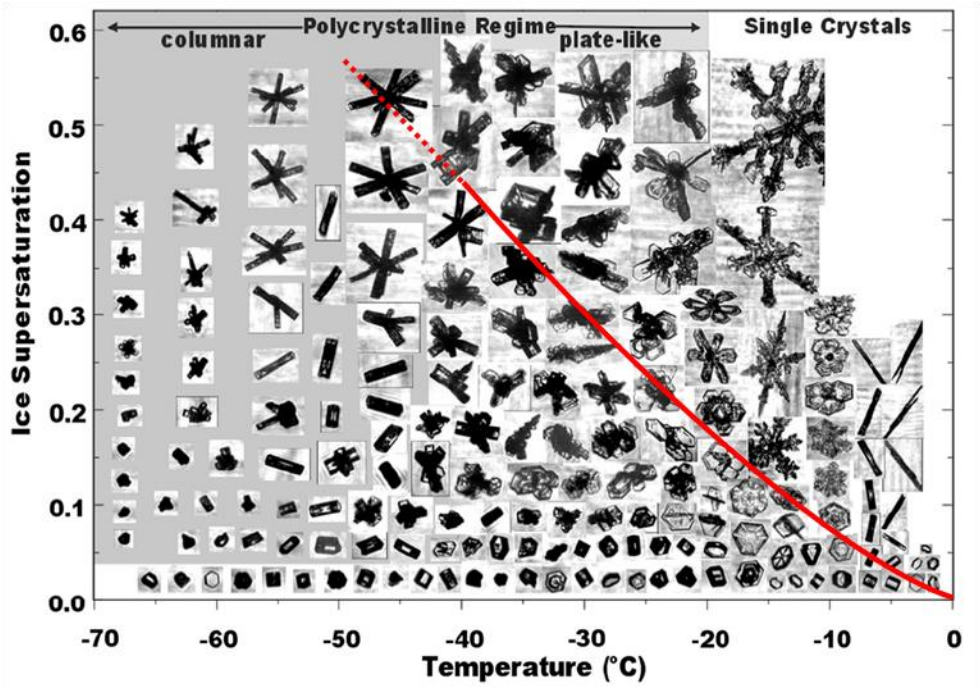

Figure 2. The detailed crystal habit diagram, with temperature and humidity dependence, from Bailey and Hallett (2009). The red line represents water saturation with sub- to the left and super- to the right.

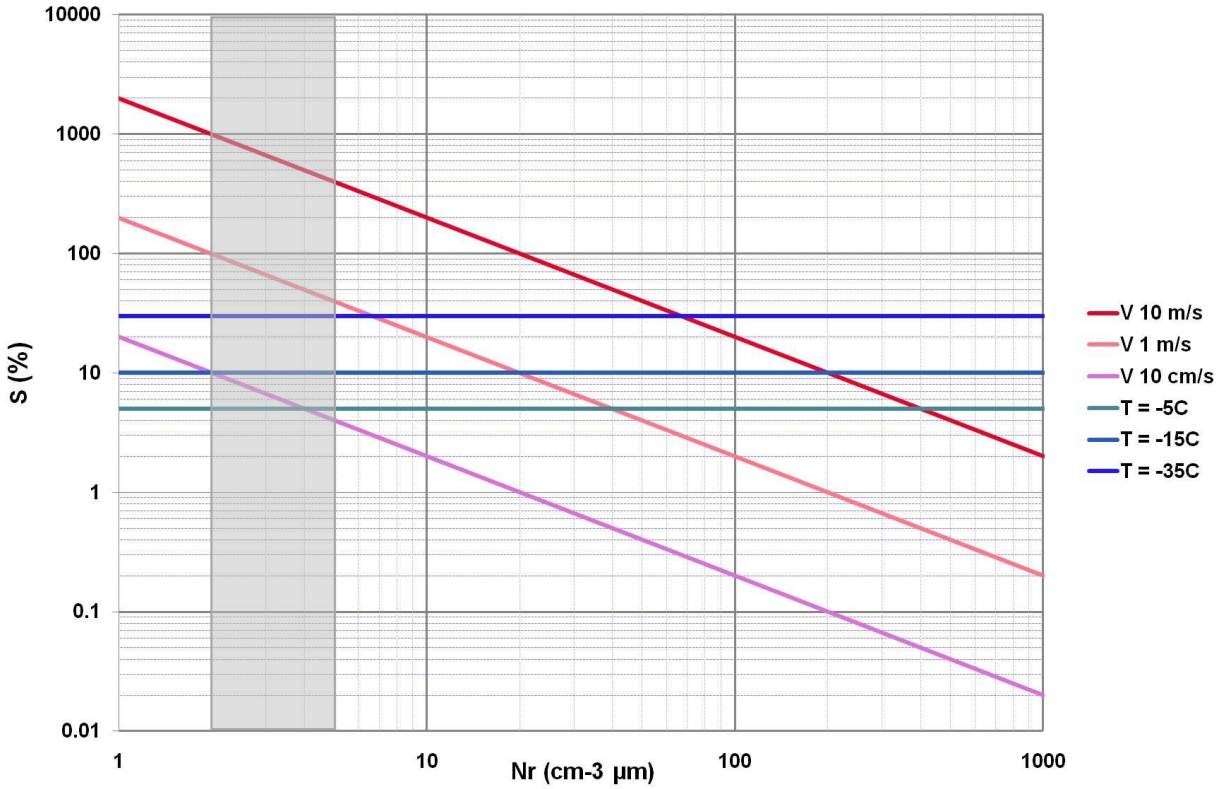

Figure 3. Updraft requirements for conditions of ice supersaturation and water supersaturation (S), as a function of the concentration of growth sites (Nr). The grey-shaded region represents the range of values of the Nr parameter measured by aircraft in regions where radar measurements suggest Category A behavior. Adapted from Korolev and Mazin Figure 5.

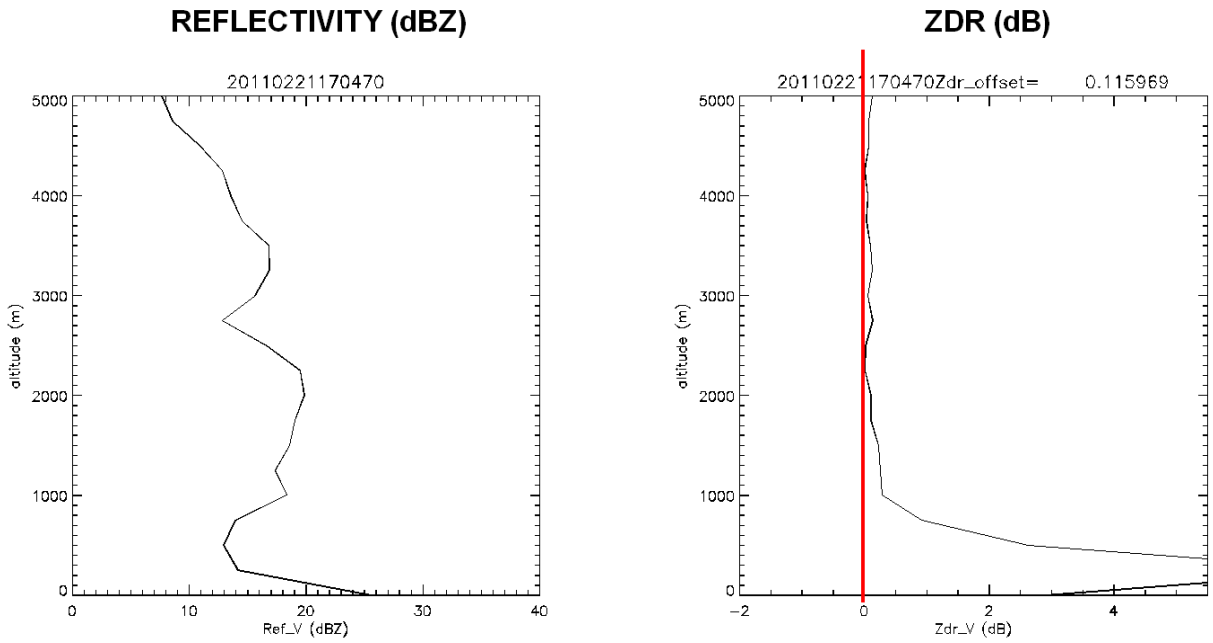

Figure 4. Sample differential reflectivity (ZDR) calibration run in vertically pointing mode on stratiform precipitation with the Valparaiso C-band polarimetric radar.

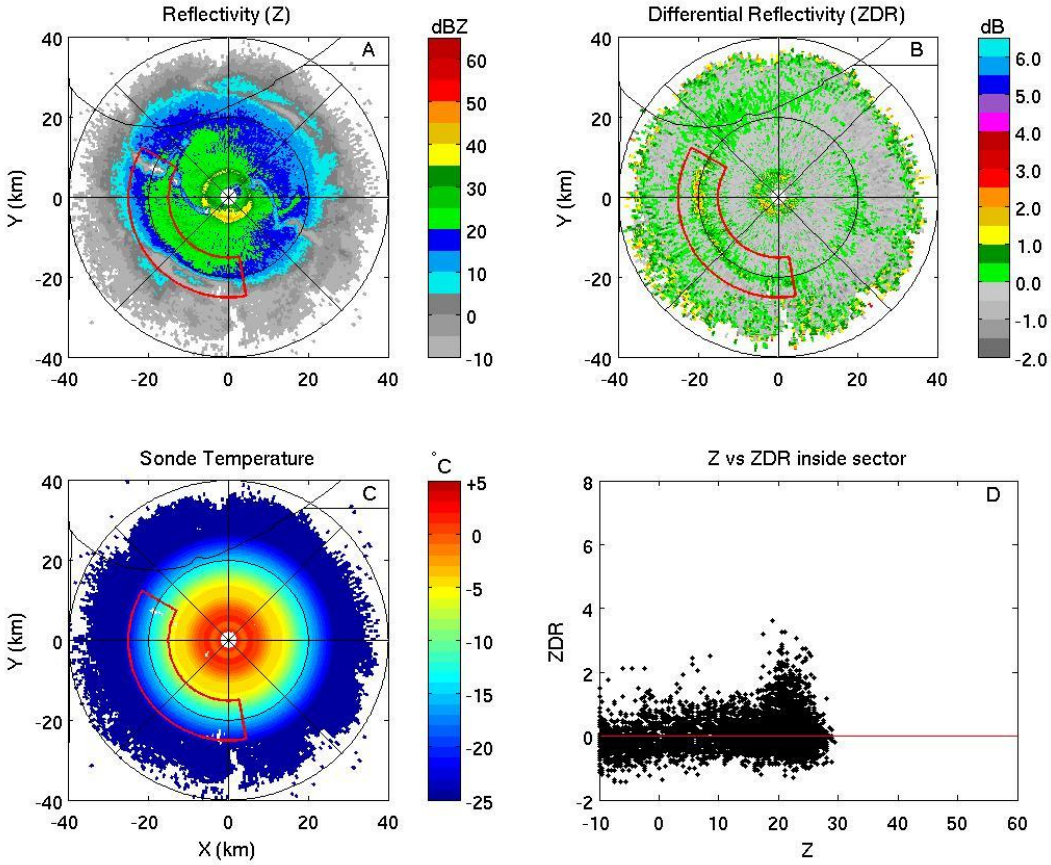

Figure 5. Plan Position Indicator (PPI) plots of reflectivity (A), differential reflectivity (B), sonde temperatures mapped to the PPI altitudes (C), and Z-ZDR scatter plot (D) for the red-outlined sector in A-C. Data are from the Valparaiso C-band polarimetric radar and a local-release weather sonde on December 8, 2009 at 2357 UTC for the 14^{o} PPI. This case is a snowstorm classified as Category A (see text).

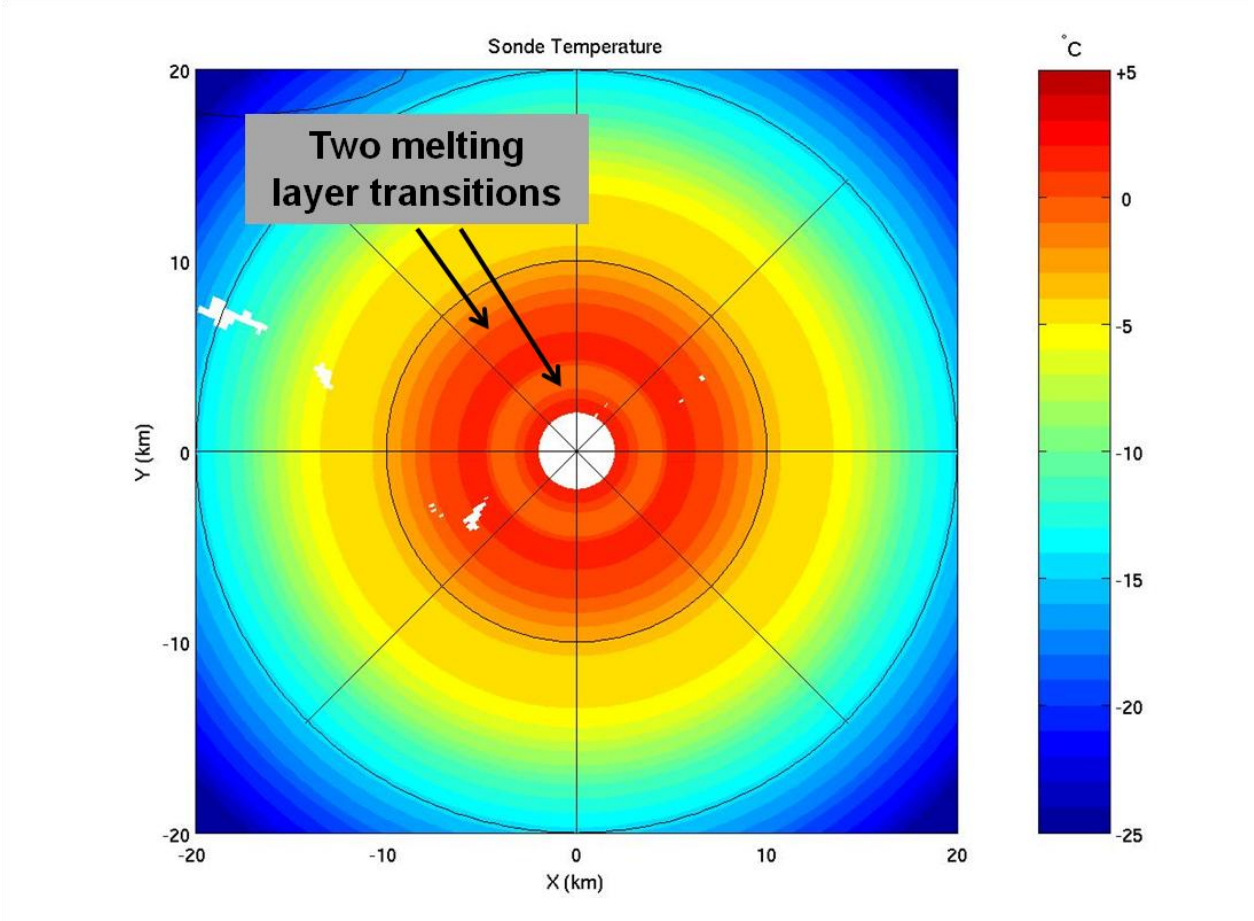

Figure 5a. Zoomed PPI plot of sonde temperatures mapped to the PPI altitudes from panel C of Figure 5. Data are for Valparaiso, IN from a local-release weather sonde on December 8, 2009 at 2357 UTC mapped to the 14^{o} PPI. Notice the two, distinct melting layer transitions between above/below freezing.

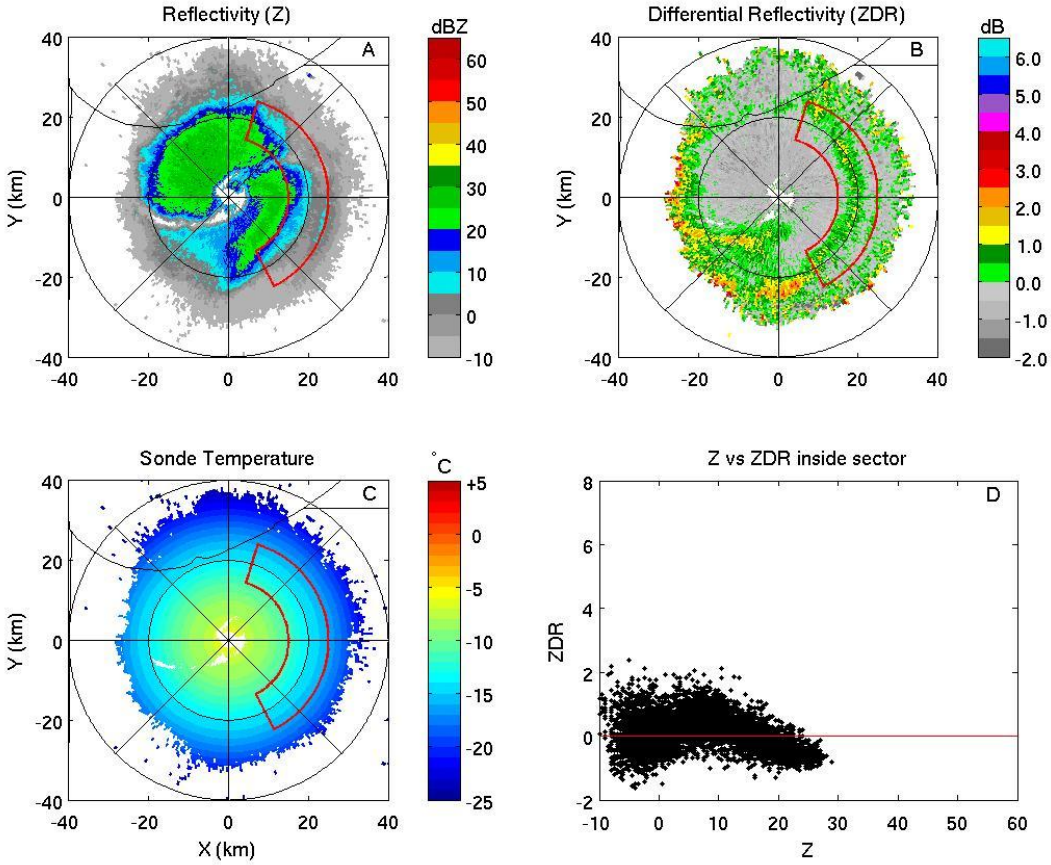

Figure 6. Plan Position Indicator (PPI) plots of reflectivity (A), differential reflectivity (B), sonde temperatures mapped to the PPI altitudes (C), and Z-ZDR scatter plot (D) for the red-outlined sector in A-C. Data are from the Valparaiso C-band polarimetric radar and a local-release weather sonde on February 24, 2010 at 1859 UTC for the 4.3^{o} PPI. This case is a snowstorm classified as Category A (see text).

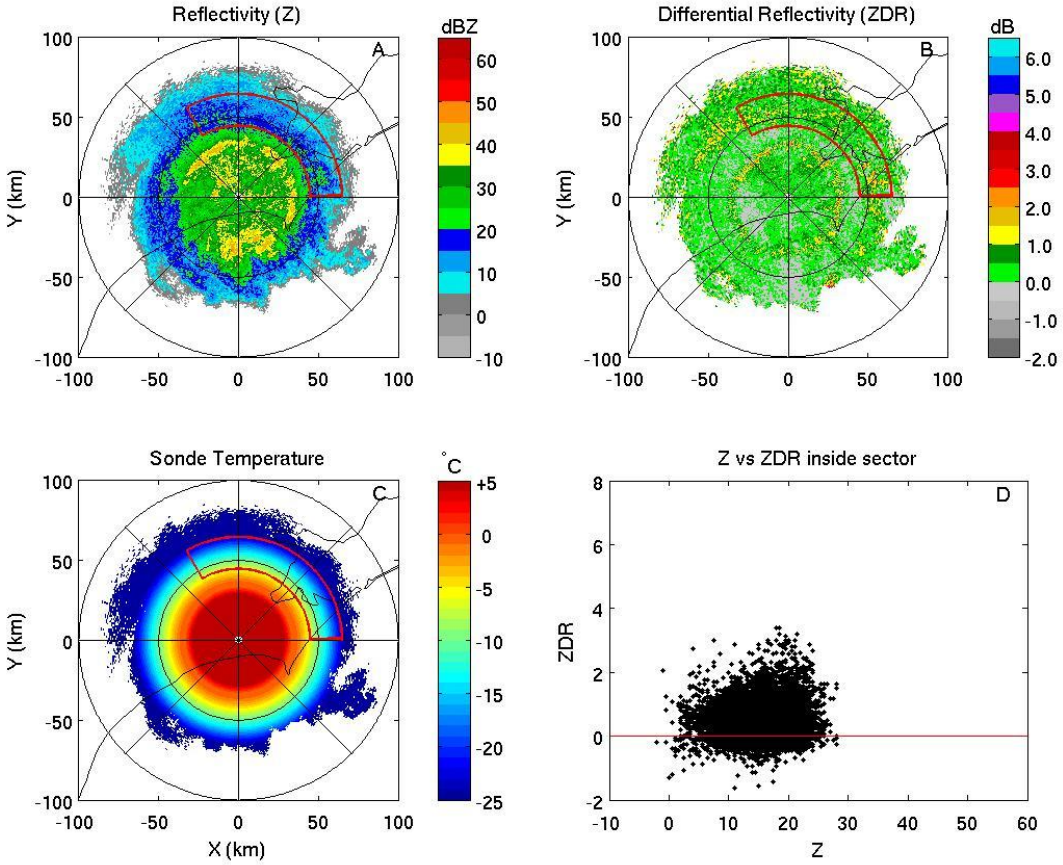

Figure 7. Plan Position Indicator (PPI) plots of reflectivity (A), differential reflectivity (B), sonde temperatures mapped to the PPI altitudes (C), and Z-ZDR scatter plot (D) for the red-outlined sector in A-C. These Hurricane Irene data are from the KMHX Morehead City, NC NEXRAD polarimetric radar and a local-release weather sonde on August 27, 2011 at 0043 UTC for the 8^{o} PPI. This case is a 'snowstorm aloft' in the hurricane and is classified as Category A (see text).

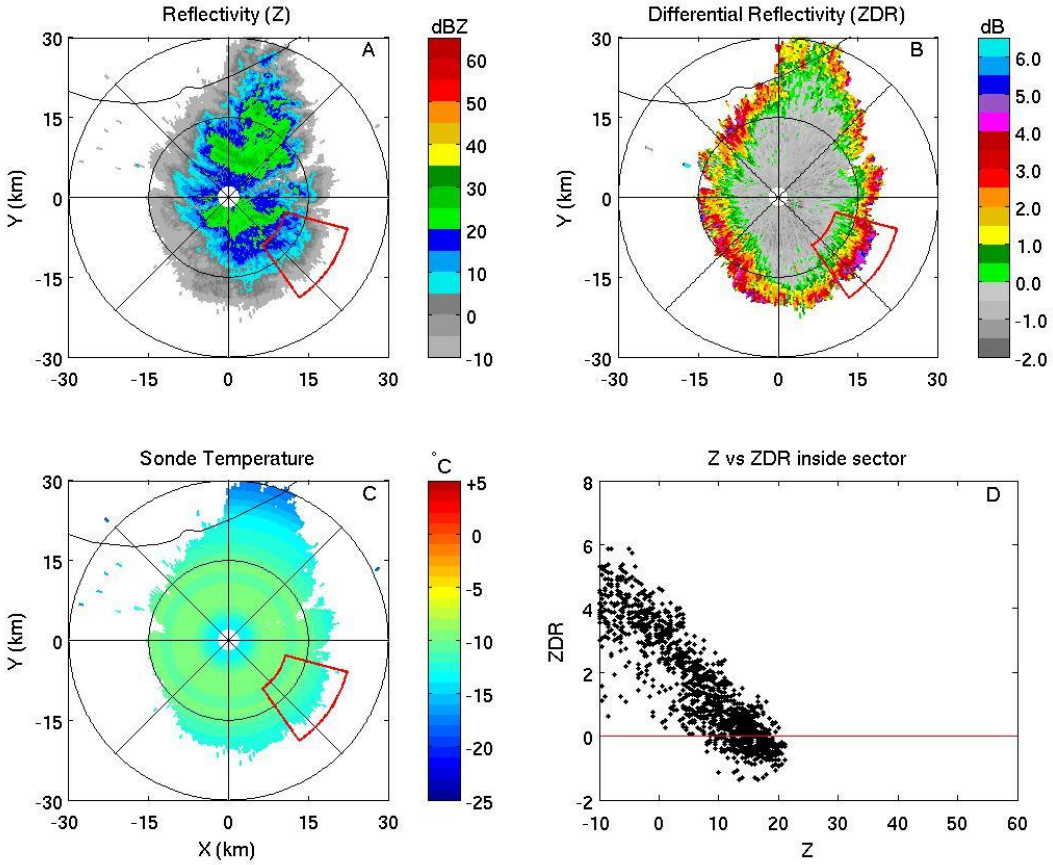

Figure 8. Plan Position Indicator (PPI) plots of reflectivity (A), differential reflectivity (B), sonde temperatures mapped to the PPI altitudes (C), and Z-ZDR scatter plot (D) for the red-outlined sector in A-C. Data are from the Valparaiso C-band polarimetric radar and a local-release weather sonde on January 8, 2010 at 1625 UTC for the 4.3^{o} PPI. This case exhibits a cocoon/edge and is classified as Category B (see text).

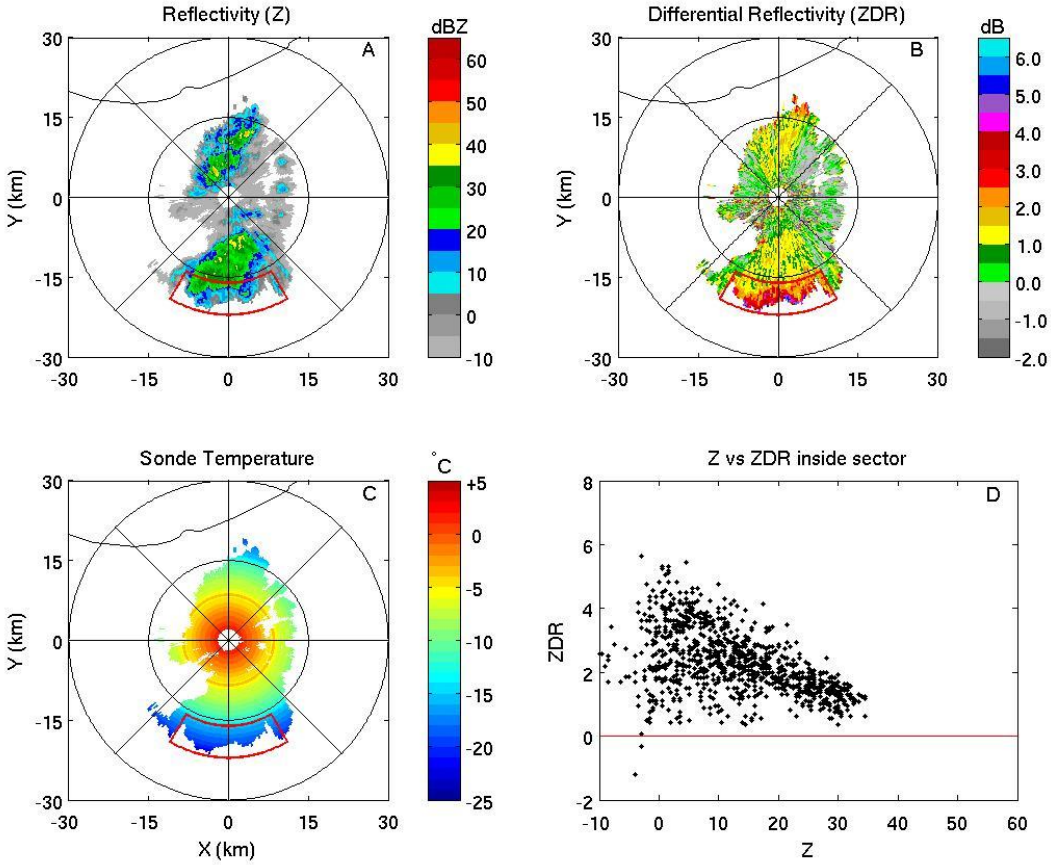

Figure 9. Plan Position Indicator (PPI) plots of reflectivity (A), differential reflectivity (B), sonde temperatures mapped to the PPI altitudes (C), and Z-ZDR scatter plot (D) for the red-outlined sector in A-C. Data are from the Valparaiso C-band polarimetric radar and a local-release weather sonde on November 5, 2010 at 0514 UTC for the 10^{o} PPI. This case is for the edge of rain showers and is classified as Category B (see text).

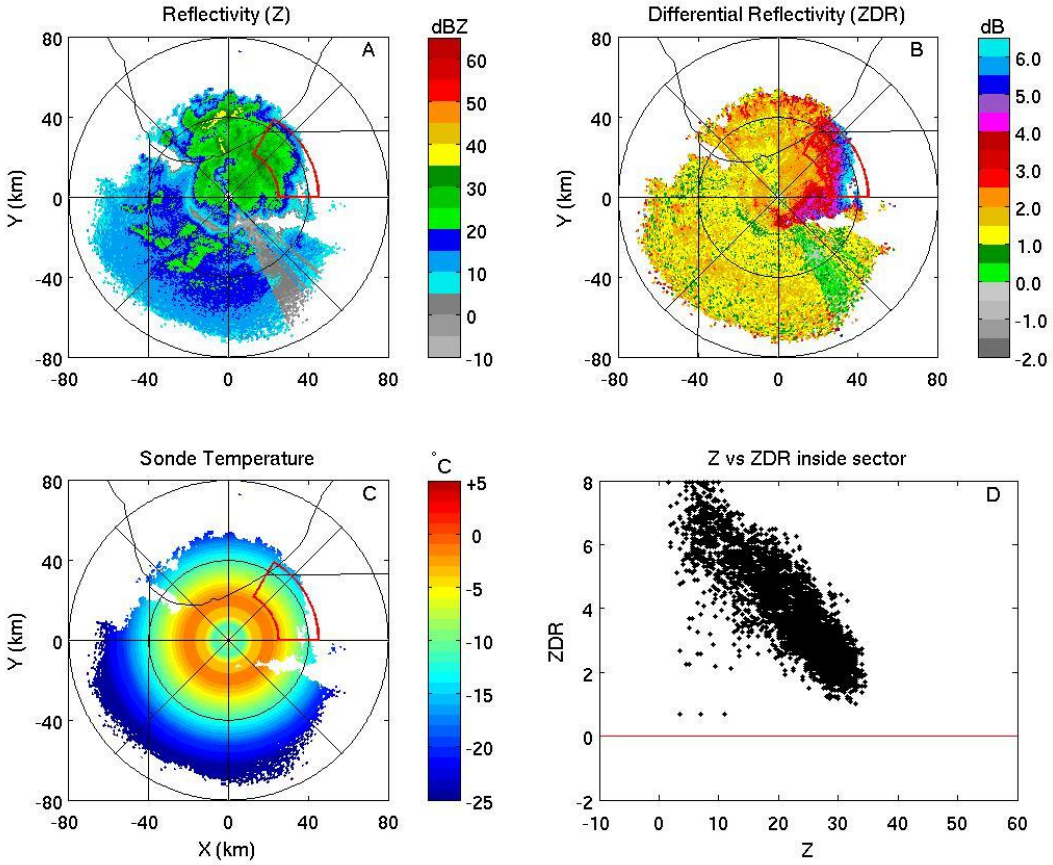

Figure 10. Plan Position Indicator (PPI) plots of reflectivity (A), differential reflectivity (B), sonde temperatures mapped to the PPI altitudes (C), and Z-ZDR scatter plot (D) for the red-outlined sector in A-C. Data are from the Valparaiso C-band polarimetric radar and a local-release weather sonde on February 1, 2011 at 1912 UTC for the 4.3^{o} PPI. This case is the leading edge of a snowstorm and is classified as Category B (see text).

APPENDIX A

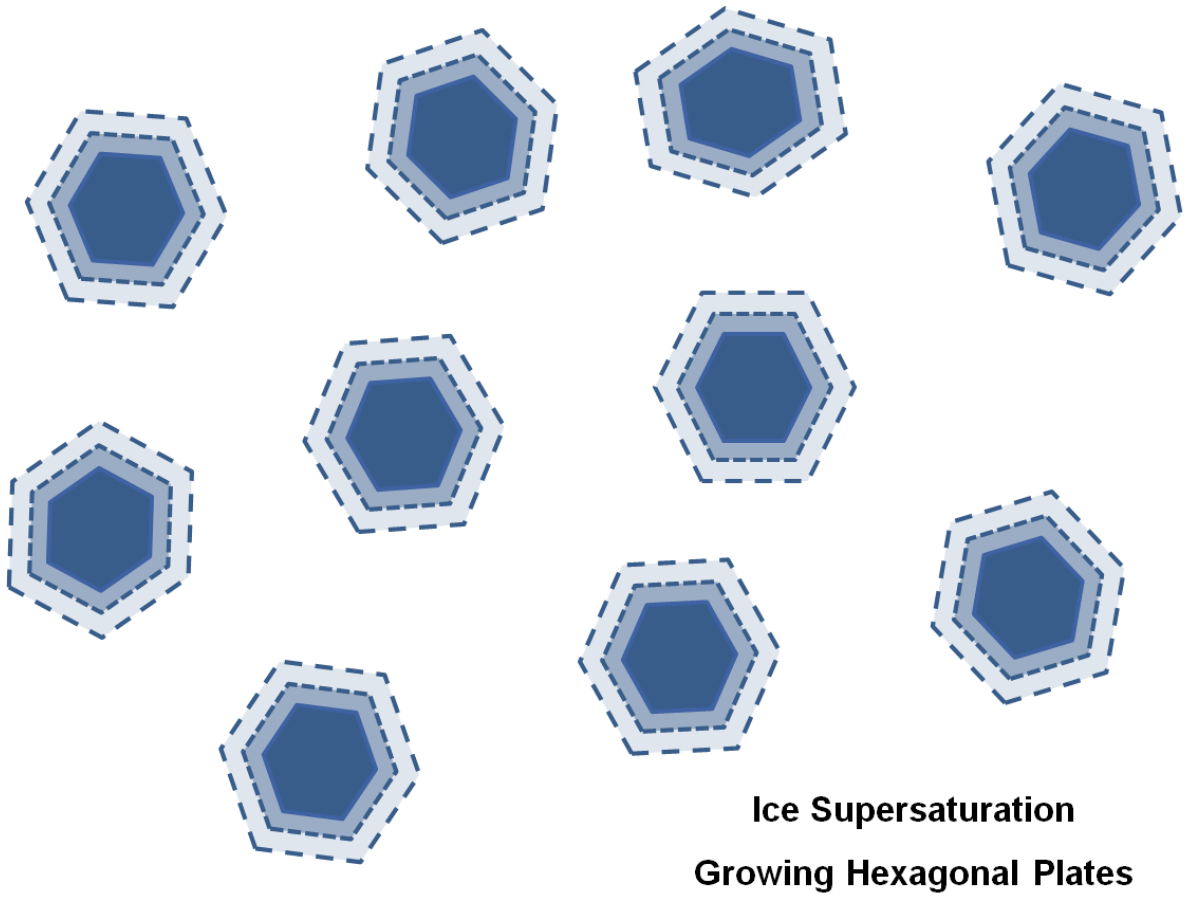

Figure A1. Illustration of microphysical situation pertaining to growth of plate crystals at ice-supersaturation and without the presence of supercooled water (Category B). The growing hexagonal plates are indicated by the dashed lines.

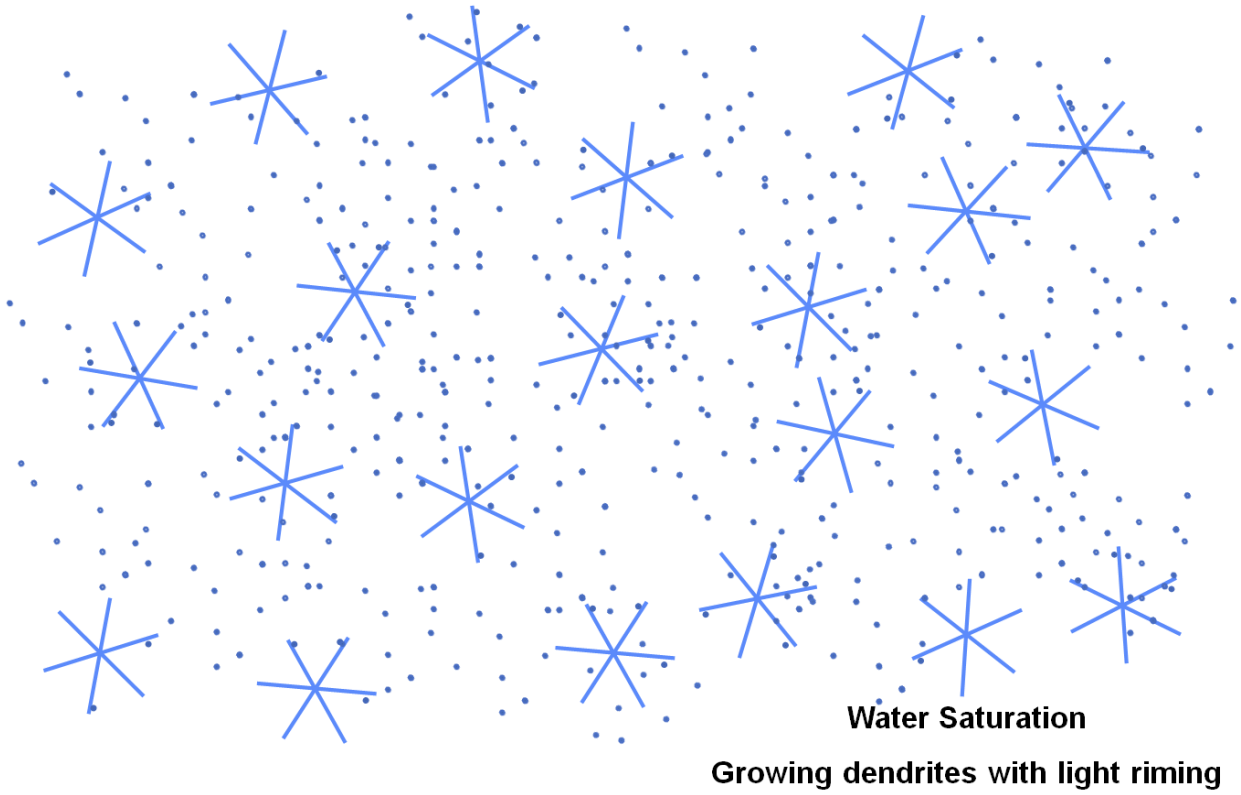

Figure A2. Illustration of microphysical situation pertaining to growth of dendrite crystals at water supersaturation and, so, in the presence of supercooled water and possible riming (Category A). The star shapes represent dendrites. The dots represent supercooled water drops/droplets. Riming occurs when the drops/droplets encounter dendrites.

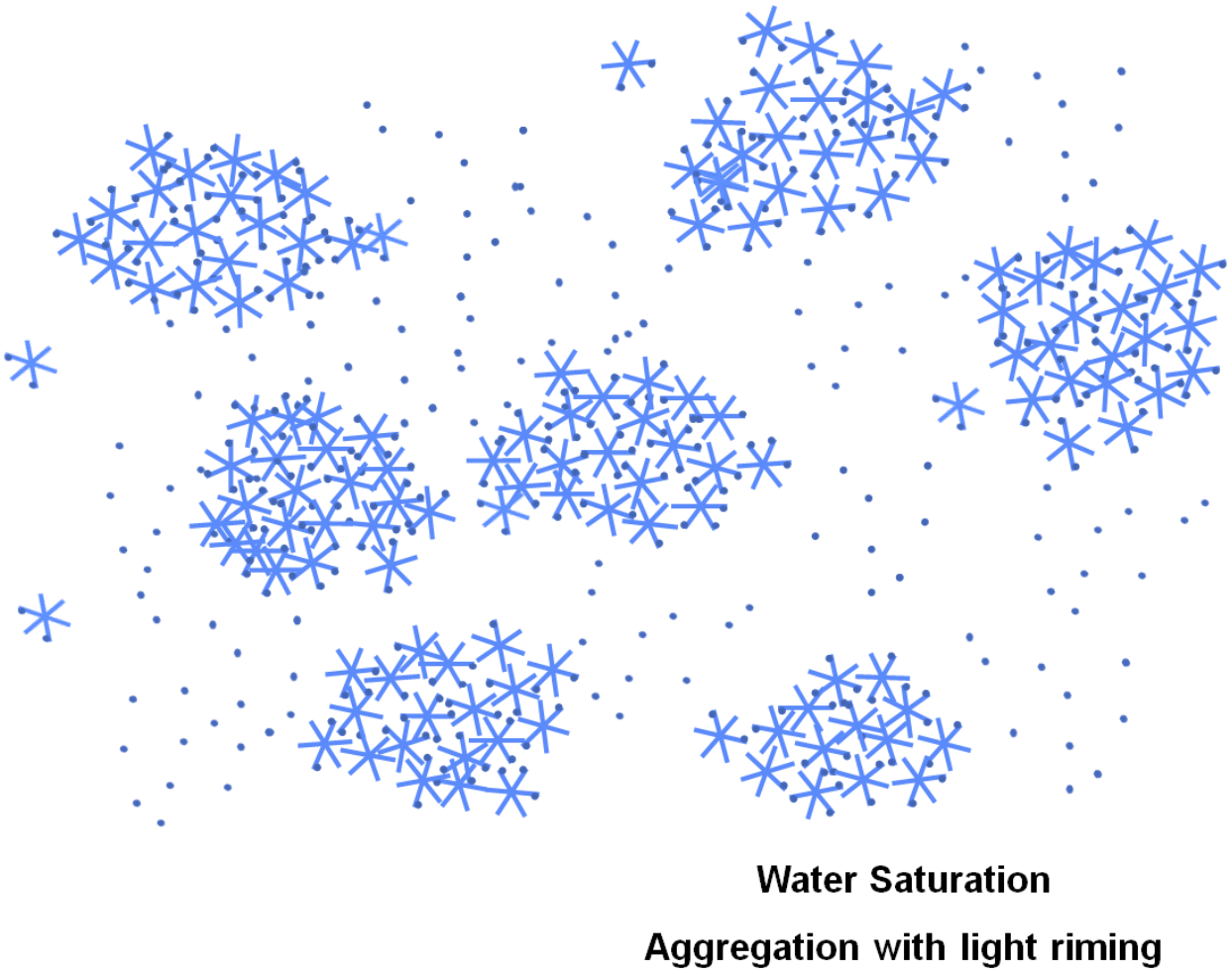

Figure A3. Illustration of microphysical situation pertaining to the aggregation of crystals with or without a riming process. Aggregation will dilute the ZDR signal.